A phase field method to simulate crack nucleation and propagation in strongly heterogeneous materials from direct imaging of their microstructure

T.T. Nguyen, Julien Yvonnet, Qi-Zhi Zhu, Michel Bornert, Camille Chateau

A phase field method to simulate crack nucleation and propagation in strongly heterogeneous materials from direct imaging of their microstructure

T.T. Nguyen [a,b], J. Yvonnet [a,*], Q.-Z. Zhu [a], M. Bornert [b], C. Chateau [b],

[a] *Université Paris-Est, Laboratoire Modélisation et Simulation Multi Échelle MSME UMR 8208 CNRS, 5 bd Descartes, F-77454 Marne-la-Vallée, France.*

[b] *Université Paris-Est, Laboratoire Navier, CNRS UMR8205, ENPC, IFSTTAR, 6 et 8 avenue Blaise Pascal, 77455 Marne-la-Vallée Cedex, France.*

Abstract

In this work, crack initiation and propagation in 2D and 3D highly heterogeneous materials models, such as those obtained by micro-CT imagery of cementitious materials, is investigated for the first time by means of the phase field method. A shifted strain split operator algorithm is proposed to handle unilateral contact within cracks in a very efficient manner. The various advantages of the phase field method for voxel-based models are discussed. More specifically, we show that the resolution related to the initial image and thus to meshes for discretizing the same microstructure does not significantly affect the simulated crack path.

Key words: Cracks, Phase Field, Nucleation, microtomography, voxel models, heterogeneous materials

1 Introduction

The numerical simulation of crack propagation in highly heterogeneous materials is a very challenging problem. Recently, the use of experimental techniques such as X-ray microtomography [19] has allowed to construct realistic

* Correspondance to J. Yvonnet
Email address: julien.yvonnet@univ-paris-est.fr (J. Yvonnet).

microstructural models of material like concrete, biological tissues (cortical bones), or composites, among many others. Developing damage models for these highly heterogeneous materials taking into account the real microstructure offers new avenues to predict more accurately fracture processes in related structures and is of formidable interest in engineering.

Unfortunately, because of the possible occurrence of multiple arbitrary branching cracks in such materials, several obstacles remain to develop reliable simulation methods of fracture nucleation and propagation in highly complex heterogeneous materials. On one hand, the classical treatment of quasi-static and dynamic fracture based on the classical Griffith theory [24,22,25,26] fails to describe crack nucleation or crack branching. Furthermore, the sharp representation of cracks requires the identification of a crack growth law, which is a complex task in the general case. On the other hand, many numerical simulation methods for crack propagation have been developed in the recent decades, but each faces well-known issues and drawbacks: (i) direct tracking of the crack front, using classical theory of brittle fracture, requires very complex remeshing algorithms [30], which are hardly tractable for complex 3D morphologies, or multiple crack fronts. The problem can be alleviated by means of recent local/global meshes superposition [33]; (ii) classical smeared crack models [32,51] suffer from inherent mesh sensitivity, which can be partially circumvented with nonlocal averaging schemes [49], or implicit gradient models [47]; (iii) methods relying on local enrichment to avoid remeshing, like the extended finite element method (XFEM) [43,5,18] require the use of a level-set function [46] to describe the geometry of the crack, inducing difficulties for crack nucleation, crack branching, and is very cumbersome for multiple crack fronts. Applications and developments of XFEM for 3D fracture problems can be found e.g. in [44,23,55,29] and in [28] in a multiscale framework; (iv) cohesive elements (see e.g. [57,15,58]) can deal with multiple crack fronts and crack nucleation, but imply the cracks to follow the elements, and suffer from convergence issues with refined meshes; finally (v), we mention a new method, called Thick Level-Set method (TLS) [7,16] in which a level-set function is employed to separate the undamaged zone from the damaged one, and where the crack is a consequence of the damage front motion, allowing crack initiation.

Recently, a new approach for the description of crack propagation has been developed. Starting from the pioneering works of Francfort and Marigo [20], difficulties arising in the classical fracture framework can be overcome by a variational-based energy minimization framework for brittle fracture (see also [10,48,9,14,4]). An important ingredient of the method relies on a regularized description of the discontinuities related to the crack front: the surface of the crack is replaced by a smooth function, using a Mumford-Shah functional [45], the original functional being substituted by an Ambrosio-Tortorelli approximation [2,3]. It has been shown that the solution of the associated variational

problem converges to the solution of the sharp crack description implying discontinuities, in the $\Gamma-$ convergence sense [36,12,13]. The approximation then regularizes a sharp crack surface topology in the solid by a scalar auxiliary variable, interpreted as a phase field describing broken and unbroken parts of the solid. Such a method has the quality that it does not require any prescription of the shape geometry and allows crack nucleation and branching, providing a very robust framework for crack propagation simulation. It has been adapted to quasi-static fracture problems in [9,8], dynamic crack propagation [11,27], and in a multiphysic context in [39,1]. Remarkably, the regularized model may be regarded as a damage model of the gradient type [34,35,6,47,21] with critical differences in the choice of the free energy and dissipation function. Recently, the problem of cohesive fracture has been reformulated in the context of phase field [56].

In this work, crack propagation in highly heterogeneous microstructures, such as segmented X-ray CT images of real materials, which are used as direct input of the simulations, is investigated for the first time by means of the phase field method, which here follows the algorithmic framework proposed by Miehe et al. [37,40]. To increase the computational efficiency of the method, a modified shifted algorithm has been introduced, to compute the strain tensor split, leading to a very simple and fast algorithm. The advantages of such an approach are demonstrated for crack nucleation and propagation in voxel-based models. Several applications to 2D and 3D images of porous cement-based materials are provided.

The overview of the paper is as follows. In sections 2 and 3, the main idea and thermodynamic foundations of the phase field method such as presented in Miehe et al. [37,40] are reviewed. In section 4, the computational and algorithmic framework based on finite elements is presented. A shifted strain tensor split algorithm is introduced to simplify the treatment of damage, assumed to be only induced by the tensile strain, to provide an efficient algorithm. Finally, numerical examples are presented in section 5.

2 Regularized representation of free discontinuities

Let $\Omega \subset \mathbb{R}^D$ be an open domain describing a cracked solid, with D being the space dimension and $\partial\Omega$ its boundary. Let Γ be a curve of dimension $D-1$ within Ω (see Fig. 2). In a regularized framework, the crack geometry is approximated by a smeared representation defined by a scalar parameter $d(\mathbf{x})$, $\mathbf{x} \in \Omega$, taking a unit value on Γ and vanishing away from it. It can be shown (see e.g. [37]) that such a function can be determined by solving the

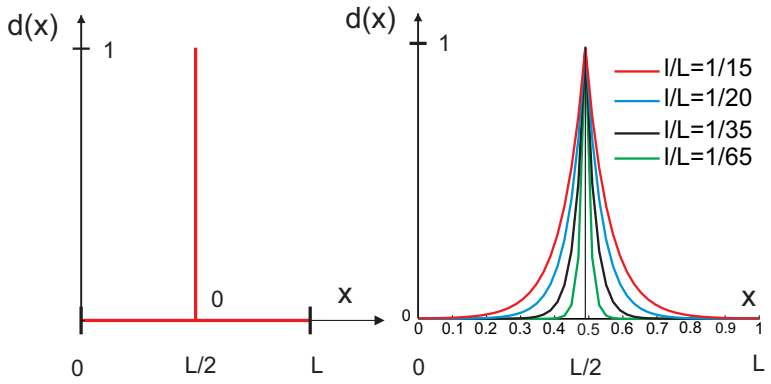

Figure 1. Regularized representation of a crack: one dimensional case: (a) sharp crack model, taking unitary value of $d(x)$ at $x = x_\Gamma = L/2$ (crack); (b) regularized representation through phase field.

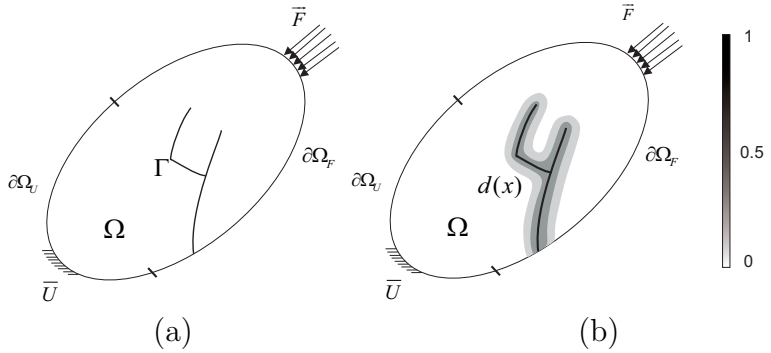

Figure 2. Regularized representation of a crack: two-dimensional case: (a) sharp crack model; (b) regularized representation through phase field.

following boundary value problem on Ω:

$$\begin{cases} d - l^2 \triangle d = 0 \ \text{ in } \Omega, \\ d(\mathbf{x}) = 1 \ \text{ on } \Gamma, \\ \nabla d(\mathbf{x}) \cdot \mathbf{n} = 0 \ \text{ on } \partial\Omega, \end{cases} \tag{1}$$

where $\Delta(.)$ is the Laplacian, l is a regularization parameter describing the actual width of the smeared crack, and $\mathbf{n}$ the outward normal to $\partial\Omega$. A one-dimensional illustration of this concept is depicted for different widths l in Fig. 1. In two and three dimensions, the solution of (1) produces a smooth representation of the crack morphology (see Fig. 2 (b)). It can be shown that (1) is the Euler-Lagrange equation associated with the variational problem:

$$d(\mathbf{x}) = Arg \left\{ \inf_{d \in \mathcal{S}_d} \Gamma_l(d) \right\}, \tag{2}$$

with $\mathcal{S}_d = \{d | d(\mathbf{x}) = 1 \text{ on } \Gamma \ \forall \mathbf{x} \in \Gamma\}$ and where

$$\Gamma_l(d) = \int_\Omega \gamma(d, \nabla d) d\Omega \tag{3}$$

represents the total crack length. In (3), $\gamma(d)$ denotes the crack density function per unit volume, defined by:

$$\gamma(d, \nabla d) = \frac{1}{2l} d^2 + \frac{l}{2} \nabla d \cdot \nabla d. \tag{4}$$

The $\Gamma-$ limit [12] of the principle (7) gives:

$$\lim_{l \to 0} \left\{ \operatorname*{Inf}_{d \in \mathcal{S}_d} \Gamma_l(d) \right\} = |\Gamma| \,. \tag{5}$$

We introduce the functional derivative $\delta\gamma(d)$ such that:

$$D_{\delta d} \Gamma_l(d) = \int_\Omega \gamma(d, \nabla d) \ \delta d \ d\Omega \tag{6}$$

where

$$D_{\delta d} \Gamma_l(d) = \left\{ \frac{d}{d\alpha} \left(\Gamma_l \left(d + \alpha \ \delta d \right) \right) \right\}_{\alpha = 0} \tag{7}$$

is the Gâteaux or directional derivative. By applying the divergence theorem to the relation (34), and assuming $\nabla d \cdot \mathbf{n} = 0$ on $\partial\Omega$ (see similar developments in section 4.1.1) it follows that:

$$\delta\gamma(d) = \frac{d}{l} - l\Delta d. \tag{8}$$

3 Review of the Phase Field method

3.1 Regularized variational framework

The variational approach to fracture mechanics provided by Francfort and Marigo [20] introduces the following energy functional for cracked body:

$$E(\mathbf{u}, \Gamma) = E_u(\mathbf{u}, \Gamma) + E_s(\Gamma) = \int_{\Omega \backslash \Gamma} W_u(\boldsymbol{\varepsilon}(\mathbf{u})) d\Omega + g_c \mathcal{H}^{d-1}(\Gamma) \tag{9}$$

where W_u is the energy density function, $\boldsymbol{\varepsilon} = \frac{1}{2} \left(\nabla \mathbf{u} + \nabla \mathbf{u}^T \right)$, $\mathbf{u}$ is the displacement field, g_c is the fracture toughness, and $\mathcal{H}^{d-1}$ is the Hausdorff surface measure giving the crack length ($d = 2$) or surface ($d = 3$). The term

$E_u(\mathbf{u}, \Gamma)$ represents the elastic energy stored in the cracked body, and $E_s(\Gamma)$ is the energy required to create the crack according to the Griffith criterion. Then, the state variables are the displacement field $\mathbf{u}$ and the geometry of the crack Γ. In a regularized framework (phase field method), the above functional is substituted by the functional:

$$E(\mathbf{u}, d) = \int_\Omega W_u(\boldsymbol{\varepsilon}(\mathbf{u}), d) d\Omega + g_c \int_\Omega \gamma(d) d\Omega, \tag{10}$$

where $\gamma(d)$ is defined by (4). The total energy is then rewritten as $E = \int_\Omega W d\Omega$ in which

$$W = W_u(\boldsymbol{\varepsilon}(\mathbf{u}), d) + g_c \gamma(d) \tag{11}$$

can be identified as the free energy.

3.2 Basics of thermodynamics and evolution of phase field

Assuming isothermal process, the Clausius-Duhem inequality states that:

$$\phi = \boldsymbol{\sigma} : \dot{\boldsymbol{\varepsilon}} - \dot{W} \geq 0 \tag{12}$$

where $\boldsymbol{\sigma}$ is the Cauchy stress and ϕ is the dissipation. We can re-write (12) as:

$$\boldsymbol{\sigma} : \dot{\boldsymbol{\varepsilon}} - \frac{\partial W}{\partial \boldsymbol{\varepsilon}} : \dot{\boldsymbol{\varepsilon}} - \frac{\partial W}{\partial d} \dot{d} = \left(\boldsymbol{\sigma} - \frac{\partial W}{\partial \boldsymbol{\varepsilon}} \right) : \dot{\boldsymbol{\varepsilon}} - \frac{\partial W}{\partial d} \dot{d} \geq 0. \tag{13}$$

It follows that if no damage occurs, i.e. for $\dot{d} = 0$, then $\phi = 0$ and

$$\sigma = \frac{\partial W}{\partial \boldsymbol{\varepsilon}}. \tag{14}$$

A reduced form of the Clausius-Duhem inequality can be re-written as:

$$\mathcal{A}\dot{d} \geq 0 \tag{15}$$

where $\mathcal{A} = -\frac{\partial W}{\partial d}$ is the thermodynamic force associated with d.

At this stage, a threshold function $F(\mathcal{A})$ such that no damage occurs is assumed in the form:

$$F(\mathcal{A}) = \mathcal{A} \leq 0. \tag{16}$$

Assuming the principle of maximum dissipation then requires the dissipation $\mathcal{A}\dot{d}$ to be maximum under the constraint (16). Using the method of Lagrange

multipliers and the following Lagrangian:

$$\mathcal{L} = -\mathcal{A}\dot{d} + \lambda F(\mathcal{A}) \tag{17}$$

yields the Kuhn-Tucker equations:

$$\frac{\partial \mathcal{L}}{\partial \mathcal{A}} = 0, \quad \lambda \geq 0, F \leq 0, \lambda F = 0. \tag{18}$$

The first equality in (18) gives:

$$\dot{d} = \lambda \frac{\partial F(\mathcal{A})}{\mathcal{A}} = \lambda. \tag{19}$$

Using the second inequality in (18), we obtain $\dot{d} \geq 0$. For $\dot{d} > 0$, $F = 0$ which gives:

$$F = -\frac{\partial W}{\partial d} = -\frac{\partial W_u(\mathbf{u}, d)}{\partial d} - g_c \delta \gamma(d) = 0. \tag{20}$$

3.3 Formulation for unilateral contact

In the present work, and following [38], we choose the following form for W_u, assuming isotropic elastic behavior of the body accounting for damage induced by traction only, through:

$$W_u(\mathbf{u}, d) = \Psi^+(\boldsymbol{\varepsilon}(\mathbf{u}))\{g(d) + k\} + \Psi^-(\boldsymbol{\varepsilon}(\mathbf{u})). \tag{21}$$

The strain field is decomposed into extensive and compressive modes as

$$\boldsymbol{\varepsilon} = \boldsymbol{\varepsilon}^+ + \boldsymbol{\varepsilon}^- \tag{22}$$

and

$$\Psi^+(\boldsymbol{\varepsilon}) = \frac{\lambda}{2}\left(\langle Tr(\boldsymbol{\varepsilon})\rangle_+\right)^2 + \mu Tr\left\{\left(\boldsymbol{\varepsilon}^+\right)^2\right\}, \tag{23}$$

$$\Psi^-(\boldsymbol{\varepsilon}) = \frac{\lambda}{2}\left(\langle Tr(\boldsymbol{\varepsilon})\rangle_-\right)^2 + \mu Tr\left\{\left(\boldsymbol{\varepsilon}^-\right)^2\right\}, \tag{24}$$

where

$$\boldsymbol{\varepsilon}^+ = \sum_{i=1}^{D} \left\langle \varepsilon^i \right\rangle_+ \mathbf{n}^i \otimes \mathbf{n}^i, \quad \boldsymbol{\varepsilon}^- = \sum_{i=1}^{D} \left\langle \varepsilon^i \right\rangle_- \mathbf{n}^i \otimes \mathbf{n}^i. \tag{25}$$

where ε^i and $\mathbf{n}^i$ are the eigenvalues and eigenvectors of $\boldsymbol{\varepsilon}$, i.e. satisfying $\boldsymbol{\varepsilon}\mathbf{n}^i = \varepsilon^i \mathbf{n}^i$. In (25) $\langle x\rangle_+ = (x + |x|)/2$ and $\langle x\rangle_- = (x - |x|)/2$. The degradation

function $g(d)$ in Eq. (21) is assumed to have the simple form:

$$g(d) = (1-d)^2. \tag{26}$$

The function $g(d)$ has been chosen such that $g'(1) = 0$ to guarantee that the strain energy density function takes a finite value as the domain is locally cracked (see e.g. [12]), and $g(0) = 1$ to guarantee that the material is initially undamaged, and $g(1) = 0$ for fully damage.

The small parameter $k << 1$ is introduced to maintain the well-posedness of the system for partially broken parts of the domain [37]. It follows that if $\dot{d} > 0$ then:

$$\mathcal{A} = -\frac{\partial W}{\partial d} = 2(1-d)\Psi^+ - \frac{g_c}{l}\delta\gamma(d). \tag{27}$$

where l has been defined in section 2.

As $2(1-d)\Psi^+ \geq 0$, then

$$\delta\gamma(d) \geq 0, \quad \text{if } \dot{d} > 0. \tag{28}$$

Expressing the variation of crack length:

$$\dot{\Gamma}_l = \int_\Omega \delta\gamma(d)\dot{d}d\Omega, \tag{29}$$

we can check that due to (28)

$$\dot{\Gamma}_l \geq 0, \tag{30}$$

satisfying non-reversible evolution of cracks.

In addition, to handle loading and unloading histories, Miehe et al. [37] introduced the strain history functional:

$$\mathcal{H}(\mathbf{x}, t) = \underset{\tau\in[0,t]}{max} \left\{\Psi^+(\mathbf{x}, \tau)\right\} \tag{31}$$

which is substituted to Ψ^+ in (20). For a discussion and justification of the use of this function, the reader is invited to refer to the mentioned reference. It yields the following phase field problem to be solved to evaluate the field $d(\mathbf{x}, t)$ at time t, using (8):

$$\begin{cases} 2(1-d)\mathcal{H} - \frac{g_c}{l}\left\{d - l^2\Delta d\right\} = 0 \ \text{ in } \Omega, \\ d(\mathbf{x}) = 1 \ \text{ on } \Gamma, \\ \nabla d(\mathbf{x}) \cdot \mathbf{n} = 0 \ \text{ on } \partial\Omega. \end{cases} \tag{32}$$

A viscous regularization was proposed in [37]. However, in the present work we have not used it.

4 Finite element discretization and simplified algorithm

4.1 Phase field problem

4.1.1 Weak form

Starting from $(32)_1$, multiplying by a test function δd and integrating over Ω, we obtain:

$$\int_\Omega \left\{ 2(1-d)\mathcal{H}\delta d - \frac{g_c}{l}\left(d - l^2\Delta d\right)\delta d \right\} d\Omega = 0. \tag{33}$$

Using the property:

$$(\Delta d)\ \delta d = \nabla\cdot(\nabla d\delta d) - \nabla d\cdot\nabla(\delta d) \tag{34}$$

and the divergence theorem, Eq. (33) is rewritten as:

$$\int_\Omega \left\{ 2(1-d)\mathcal{H} - \frac{g_c\ d}{l} \right\} \delta d - \int_\Omega g_c l \nabla d\cdot\nabla(\delta d)\ d\Omega$$

$$+ \int_{\partial\Omega} g_c l \nabla d\cdot\mathbf{n}\delta d\ d\Gamma = 0 \tag{35}$$

Using (32_3), we finally obtain:

$$\int_\Omega \left\{ \left(2\mathcal{H} + \frac{g_c}{l}\right) d\delta d + g_c l\nabla d\cdot\nabla(\delta d) \right\} d\Omega = \int_\Omega 2\mathcal{H}\delta d d\Omega. \tag{36}$$

In the present work, the computations are performed in quasi-static conditions. Then, the time steps introduced in the following actually refer to load increments. Introducing a time stepping, the problem to be solved at time t^{n+1} is expressed by seeking $d(\mathbf{x}) \in \mathcal{S}_d$, such that:

$$\int_\Omega \left\{ \left(2\mathcal{H}_n + \frac{g_c}{l}\right) d_{n+1}\delta d + g_c l\nabla d_{n+1}\cdot\nabla(\delta d) \right\} d\Omega = \int_\Omega 2\mathcal{H}_n\delta d d\Omega.$$

$$\forall \delta d(\mathbf{x}) \in H_0^1(\Omega). \tag{37}$$

where $\mathcal{H}_n = \mathcal{H}(\mathbf{u}_n)$ is computed from the previous load increment (load increment) by:

$$\begin{cases} \mathcal{H}_{n+1}(\mathbf{x}) = \Psi^+_{n+1}(\mathbf{x}) \quad \text{if } \Psi^+_{n+1}(\mathbf{x}) > \Psi^+_n(\mathbf{x}), \\ \mathcal{H}_{n+1}(\mathbf{x}) = \Psi^+_n(\mathbf{x}) \quad \text{if } \Psi^+_{n+1}(\mathbf{x}) \leq \Psi^+_n(\mathbf{x}). \end{cases} \tag{38}$$

Note that Eq. (38) is the algorithmic counterpart of Eq. (31).

4.1.2 FEM discretization of phase field problem

In this work, 2D and 3D problems are considered. For 2D problems, a mesh of linear 3-node triangles has been employed, while for 3D problems regular meshes with 8-node trilinear elements have been used. For the sake of clarity, only 2D FEM discretization is detailed. The phase field and phase field gradient are approximated in one element by

$$d(\mathbf{x}) = \mathbf{N}_d(\mathbf{x})\mathbf{d}_i \quad \text{and} \quad \nabla d(\mathbf{x}) = \mathbf{B}_d(\mathbf{x})\mathbf{d}_i, \tag{39}$$

where $\mathbf{d}_i$ are the nodal values of $\mathbf{d}_{n+1}$.

The same discretization is employed for the variations:

$$\delta d(\mathbf{x}) = \mathbf{N}_d(\mathbf{x})\delta\mathbf{d}_i \quad \text{and} \quad \nabla\delta\mathrm{d}(\mathbf{x}) = \mathbf{B}_\mathrm{d}(\mathbf{x})\delta\mathbf{d}_\mathrm{i} \tag{40}$$

where $\mathbf{N}_d(\mathbf{x})$ and $\mathbf{B}_d(\mathbf{x})$ are vectors and matrices of shape functions and of shape functions derivatives for scalar fields, respectively. Introducing the above FEM discretization in (4.1.1) results into a linear system of equations:

$$\mathbf{K}_d\mathbf{d} = \mathbf{F}_d \tag{41}$$

where $\mathbf{d}$ is the vector containing all nodal phase field variables,

$$\mathbf{K}_d = \int_\Omega \{(\frac{g_c}{l} + 2\mathcal{H}_n)\mathbf{N}_d^T\mathbf{N}_d + g_c l\mathbf{B}_d^T\mathbf{B}_d\}d\Omega \tag{42}$$

and

$$\mathbf{F}_d = \int_\Omega 2\mathbf{N}_d^T\mathcal{H}_n d\Omega. \tag{43}$$

In (42), $\mathcal{H}_n$ is evaluated at the Gauss points by (38).

4.2 Displacement problem

4.2.1 Weak form

The weak form associated with the displacement problem is found by solving the variational problem:

$$\mathbf{u}(\mathbf{x}) = Arg\left\{\inf_{\mathbf{u}\in\mathcal{S}_u}\left(E(\mathbf{u},d) - W^{ext}\right)\right\} \tag{44}$$

where $\mathcal{S}_u = \{\mathbf{u}|\mathbf{u}(\mathbf{x}) = \bar{\mathbf{u}} \text{ on } \partial\Omega_u, \quad \mathbf{u} \in H^1(\Omega)\}$ and $W^{ext} = \int_\Omega \mathbf{f}\cdot\mathbf{u}d\Omega + \int_{\partial\Omega_F} \overline{\mathbf{F}}\cdot\mathbf{u}d\Gamma$ with $\mathbf{f}$ and $\overline{\mathbf{F}}$ body forces and prescribed traction over the boundary $\partial\Omega_F$. We obtain the classical weak form for $\mathbf{u}(\mathbf{x}) \in \mathcal{S}_u$:

$$\int_\Omega \boldsymbol{\sigma} : \boldsymbol{\varepsilon}(\delta\mathbf{u})d\Omega = \int_\Omega \mathbf{f}\cdot\delta\mathbf{u}d\Omega + \int_{\partial\Omega_F} \overline{\mathbf{F}}\cdot\delta\mathbf{u}d\Gamma \;\forall\delta\mathbf{u} \in H_0^1(\Omega), \tag{45}$$

where $\boldsymbol{\sigma} = \frac{\partial W_u}{\partial\boldsymbol{\varepsilon}}$ is given using (21) and (26), by:

$$\boldsymbol{\sigma} = \left((1-d)^2 + k\right)\left\{\lambda\left\langle Tr\boldsymbol{\varepsilon}\right\rangle_+ \mathbf{1} + 2\mu\boldsymbol{\varepsilon}^+\right\} + \lambda\left\langle Tr\boldsymbol{\varepsilon}\right\rangle_- \mathbf{1} + 2\mu\boldsymbol{\varepsilon}^-. \tag{46}$$

4.2.2 FEM discretization of displacement problem and shifted strain split algorithm

To avoid the nonlinearity related to the decomposition of the strain field (22)-(25) at time t^{n+1}, we introduce two shifted strain tensor split algorithms.

$$\text{Split algorithm 1}: \quad \boldsymbol{\varepsilon}^+_{n+1} \simeq \mathbb{P}^+_n : \boldsymbol{\varepsilon}_{n+1}, \quad \boldsymbol{\varepsilon}^-_{n+1} \simeq \mathbb{P}^-_n : \boldsymbol{\varepsilon}_{n+1}, \tag{47}$$

where $\mathbb{P}^\pm_n = \frac{\partial\boldsymbol{\varepsilon}^\pm_n}{\partial\boldsymbol{\varepsilon}_n}$ can be expressed thanks to the algorithm presented in Miehe and Lambrecht [38]. This algorithm seems to have been used in [37], although not explicitly described therein. Such a simplification might induce small load increments to maintain a good accuracy of the solution. To overcome this drawback, we propose a second algorithm, described as follows.

$$\text{Split algorithm 2}: \quad \boldsymbol{\varepsilon}^+_{n+1} \simeq \tilde{\mathbb{P}}^+_{n+1} : \boldsymbol{\varepsilon}_{n+1}, \quad \boldsymbol{\varepsilon}^-_{n+1} \simeq \tilde{\mathbb{P}}^-_{n+1} : \boldsymbol{\varepsilon}_{n+1}, \tag{48}$$

where

$$\begin{aligned} &\tilde{\mathbb{P}}^+_{n+1} \simeq \mathbb{P}^+_n + \Delta t_n \frac{\partial\mathbb{P}^+_n}{\partial t} \\ &\tilde{\mathbb{P}}^-_{n+1} = \mathbb{I} - \tilde{\mathbb{P}}^+_{n+1}; \end{aligned} \tag{49}$$

with $\Delta t_n = t^{n+1} - t^n$, and $\frac{\partial\mathbb{P}^+_n}{\partial t} \simeq \frac{\mathbb{P}^+_n - \mathbb{P}^+_{n-1}}{\Delta t_{n-1}}$. We then allow load increments to be adapted, as when cracks begin nucleating and propagating, smaller load

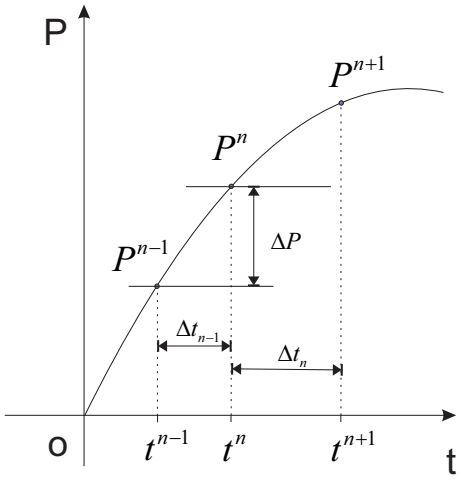

Figure 3. Evolution of the projection tensor between two load increments t^n and t^{n+1}.

increments might be required. Furthermore, in the broken zone ($d \simeq 1$), the decomposition (25) might lead unphysical values of $\boldsymbol{\varepsilon}^{\pm}$. To alleviate this issue, we introduce a weight function $\beta(d)$ such that $\beta(d=0)=0$, $\beta(d=1)=0$, e.g. $\beta(d)=(1-d)^2$:

$$\mathbb{P}^{+}_{n+1} \simeq \mathbb{P}^{+}_{n} + \beta(d_n)\Delta t_n \frac{\partial \mathbb{P}^{+}_{n}}{\partial t}. \tag{50}$$

This ensures that for $\beta(d=0)$ the behavior is linear and that the projector tensor is well defined. For $d=1$, the property $\beta(d=1)=0$ leads to compute the projector tensor as the projector from the previous load increment.

In addition, we propose the following approximations:

$$\langle Tr\boldsymbol{\varepsilon}_{n+1}\rangle_{+} \simeq \mathcal{R}^{+}(\boldsymbol{\varepsilon}_n)\, Tr\boldsymbol{\varepsilon}_{n+1}, \quad \langle Tr\boldsymbol{\varepsilon}_{n+1}\rangle_{-} \simeq \mathcal{R}^{-}(\boldsymbol{\varepsilon}_n)\, Tr\boldsymbol{\varepsilon}_{n+1}, \tag{51}$$

with

$$\mathcal{R}^{+}(\boldsymbol{\varepsilon}_n) = \frac{1}{2}\left(\mathrm{sign}\left(Tr\boldsymbol{\varepsilon}_n\right)+1\right), \quad \mathcal{R}^{-}(\boldsymbol{\varepsilon}_n) = \frac{1}{2}\left(\mathrm{sign}\left(-Tr\boldsymbol{\varepsilon}_n\right)+1\right). \tag{52}$$

A FEM discretization and the vector form for second order tensors in 2D are introduced, namely: $[\boldsymbol{\varepsilon}] = \{\varepsilon_{11};\varepsilon_{22};2\varepsilon_{12}\}^T$, $[\boldsymbol{\sigma}] = \{\sigma_{11};\sigma_{22};\sigma_{12}\}^T$, $[\mathbf{1}] = \{1;1;0\}^T$, as well as the FEM approximations $\mathbf{u}=\mathbf{N}\mathbf{u}_i$, $\delta\mathbf{u}=\mathbf{N}\delta\mathbf{u}_i$, $[\boldsymbol{\varepsilon}(\mathbf{u})] = \mathbf{B}\mathbf{u}_i$, $[\boldsymbol{\varepsilon}(\delta\mathbf{u})] = \mathbf{B}\delta\mathbf{u}_i$; $\mathbf{u}_i$ denoting nodal displacements at time t_{n+1}. Setting $\mathcal{R}^{\pm}(\boldsymbol{\varepsilon}_n) \equiv \mathcal{R}^{\pm}_n$ and $\mathbf{P}^{\pm}(\boldsymbol{\varepsilon}_n) \equiv \mathbf{P}^{\pm}_n$, where $\mathbf{P}^{\pm}$ are the matrix forms associated with the fourth-order tensors $\mathbb{P}^{\pm}$, then the stress can be expressed at time t_{n+1} by:

$$\begin{aligned}[\boldsymbol{\sigma}_{n+1}] = &\left((1-d_{n+1})^2+k\right)\left\{\lambda\mathcal{R}^{+}_n\left([\boldsymbol{\varepsilon}_{n+1}]\cdot[\mathbf{1}]\right)[\mathbf{1}] + 2\mu\mathbf{P}^{+}_n[\boldsymbol{\varepsilon}_{n+1}]\right\}\\ &+\lambda\mathcal{R}^{-}_n\left([\boldsymbol{\varepsilon}_{n+1}]\cdot[\mathbf{1}]\right)[\mathbf{1}] + 2\mu\mathbf{P}^{-}_n[\boldsymbol{\varepsilon}_{n+1}].\end{aligned} \tag{53}$$

Introducing the above FEM discretization and approximations (48)-(52) in (45), the linear system of equations is obtained:

$$\left\{\mathbf{K}_1(d_{n+1},\mathbf{u}_n)+\mathbf{K}_2(\mathbf{u}_n)\right\}\mathbf{u}_{n+1}=\mathbf{F}_{n+1} \tag{54}$$

with

$$\mathbf{K}_1(d_{n+1})=\int_\Omega \mathbf{B}^T\left\{\left((1-d_{n+1})^2+k\right)\left(\lambda\mathcal{R}_n^+\left[\mathbf{1}\right]^T\left[\mathbf{1}\right]+2\mu\mathbf{P}_n^+\right)\right\}\mathbf{B}d\Omega, \tag{55}$$

$$\mathbf{K}_2=\int_\Omega \mathbf{B}^T\left\{\lambda\mathcal{R}_n^-\left[\mathbf{1}\right]^T\left[\mathbf{1}\right]+2\mu\mathbf{P}_n^-\right\}\mathbf{B}d\Omega, \tag{56}$$

$$\mathbf{F}_{n+1}=\int_\Omega \mathbf{N}^T\mathbf{f}d\Omega+\int_{\partial\Omega_F}\mathbf{N}^T\overline{\mathbf{F}}_{n+1}d\Gamma. \tag{57}$$

We can note that such algorithms then do not require Newton linearization for the displacement problem, as in each algorithm, the computation of $\mathbb{P}^{\pm}$ is performed at the previous load increment.

4.3 Overall algorithm

The overall algorithm, involving the previously mentioned shifted strain decomposition algorithm (split algorithm 2), is described as follows.

Initialization. Initialize the displacement field $\mathbf{u}_0(\mathbf{x})$, the phase field $d_0(\mathbf{x})$, and the strain-history functional $\mathcal{H}_0=0$.

WHILE $t^{n+1}\leq T$, given $\mathbf{u}_n$, d_n and $\mathcal{H}_n$,

(1) Compute $\tilde{\mathbb{P}}^+(\boldsymbol{\varepsilon}_n)$, $\tilde{\mathbb{P}}^-(\boldsymbol{\varepsilon}_n)$, $\mathcal{R}^+(\boldsymbol{\varepsilon}_n)$ and $\mathcal{R}_-(\boldsymbol{\varepsilon}_n)$ by (50)-(52).
(2) Compute the strain history functional $\mathcal{H}_{n+1}$ by (38).
(3) Compute $d_{n+1}(\mathbf{x})$ by solving the linear phase field problem (41).
(4) Compute $\mathbf{u}_{n+1}(\mathbf{x})$ by solving the linear displacement problem problem (54).
(5) $(.)_n \leftarrow (.)_{n+1}$ and go to (1).

In the present code, the assembly of the different matrices is parallelized [17], and an iterative Biconjugate gradient stabilized solver [53] was used to solve the largest systems.

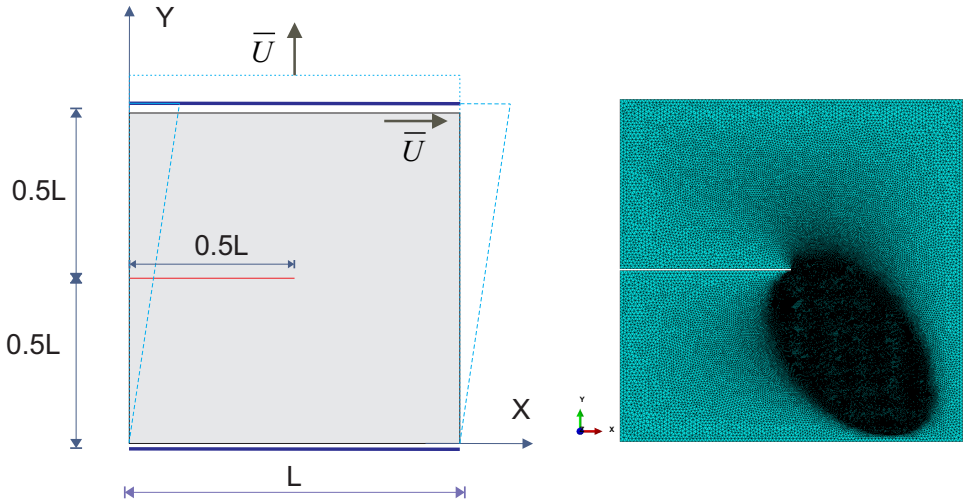

Figure 4. Shear crack propagation problem: (a) geometry and boundary conditions; (b) FEM mesh.

5 Numerical examples

5.1 Validation of the shifted tensor split algorithm: curved crack propagation in 2D

The main purpose of this first example is to validate the algorithm introduced in section 4.2.2. For this purpose, we consider the problem of curved crack propagation introduced in [37]. A square domain whose side length is $L = 1$ mm contains an initial crack, as depicted in Fig. 4. The lower end ($y = 0$) of the domain is blocked along x- and y-directions. On the upper end ($y = L$), the displacement along y is fixed to zero, while the uniform $x-$displacement $\overline{U}$ is increased with time. Due to this shear loading, a curved crack initiates and propagates.

The initial cracked domain is meshed according to the initial geometry described in Fig. 4 (a). The mesh is refined in the expected crack propagation zone, as shown in Fig. 4 (b) and involves 74124 elements. The typical size of an element in the crack propagation zone is about $h_{min} \approx 6.10^{-4}$ mm and $h_{max} = 0.02$ mm in the rest of the domain.

Plane stress is assumed. The solid is supposed to be homogeneous isotropic solid (typical of a metal) with properties $\lambda = 121.15$ GPa and $\mu = 80.77$ GPa. The fracture toughness is $g_c = 2700$ N/m [37]. Two displacement increments $\overline{U} = 10^{-5}$ mm and $\overline{U} = 2.10^{-5}$ mm have been tested, and have been prescribed for 1500 load increments. The length scale parameter is chosen as $l = 0.0075$ mm. The evolution of the crack during the simulation is shown in Fig. 5.

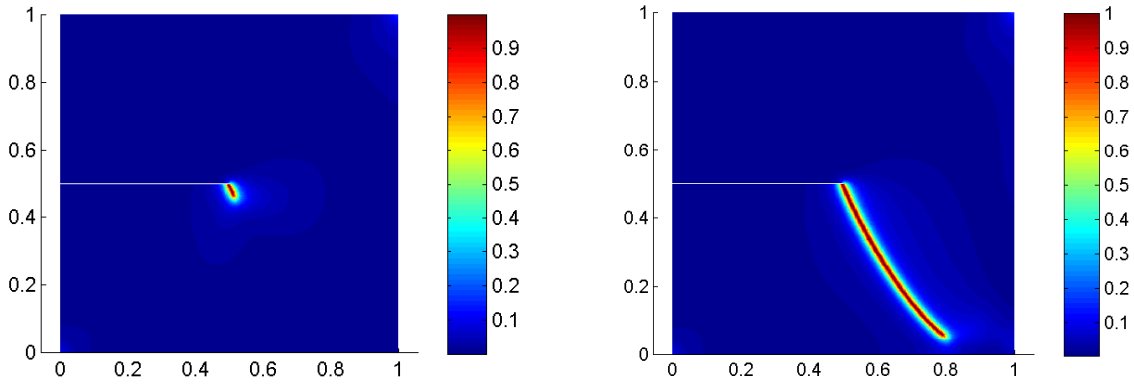

Figure 5. Phase field $d(\mathbf{x})$ distribution during crack evolution for the shear crack propagation problem for $\overline{U} = 10.10^{-3}$ mm and $\overline{U} = 13.10^{-3}$ mm.

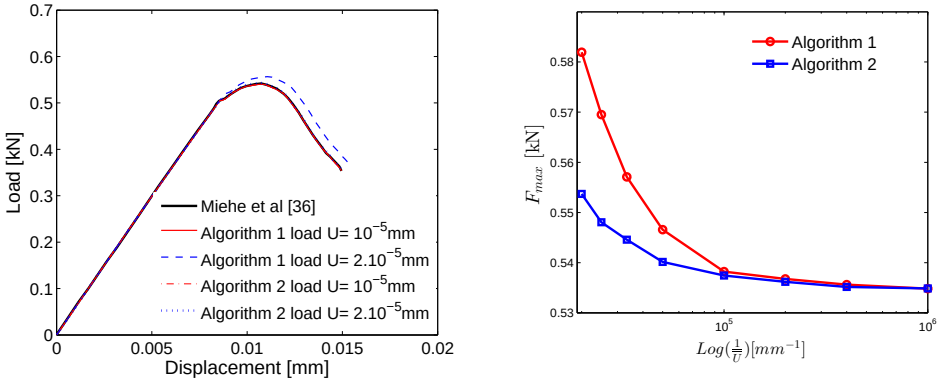

(a) (b)

Figure 6. (a) Comparison of force-displacement curve for two split algorithms; (b) convergence of the maximum load before failure with respect to the load increment for both algorithms.

To demonstrate the advantage of the proposed algorithm, we have compared the solutions provided by the two schemes defined in section 4.2.2 with the solution provided in [37], which involves viscous regularization. Then, we have computed the load-displacement curve for the two load increments mentioned above. The results are presented in Figs. 6. We can note in Fig. 6 (a) that when small load increments are used, both algorithms provide accurate solutions with respect to the reference solution of [37]. However, when larger load increments are used, the algorithm 2 maintains a more accurate solution than algorithm 1. In Fig. 6 (b), we have analyze the convergence of the maximum load before failure with respect to the load increment. It can be noted that the convergence is increased with algorithm 2, allowing larger load increments for computational saving.

Next, we investigate the convergence of the maximum load before failure with

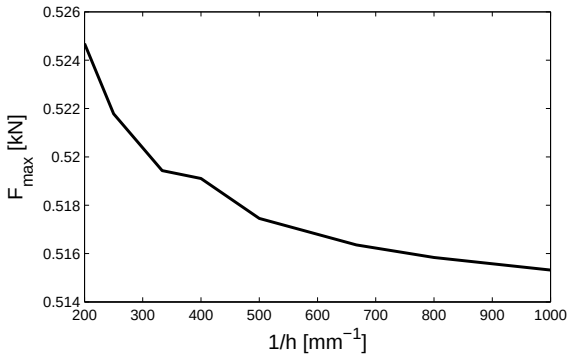

Figure 7. Convergence analysis of the maximum load before failure with respect to the mesh size.

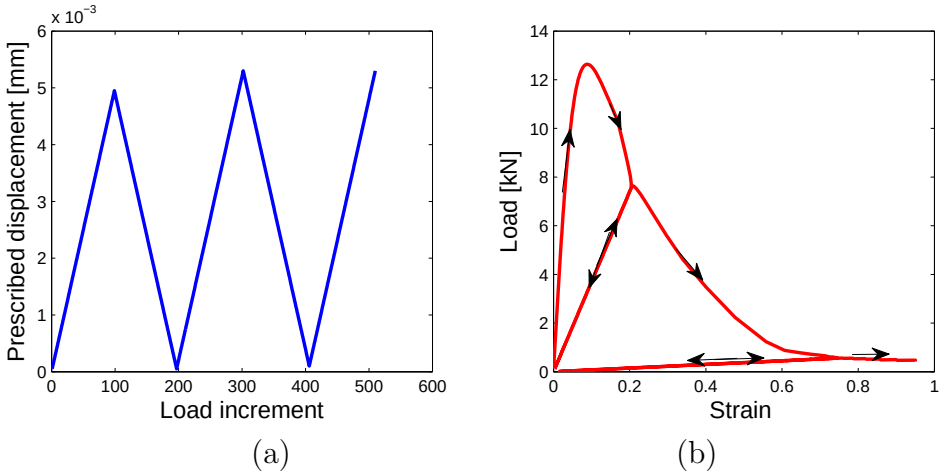

(a) (b)

Figure 8. (a) Prescribed loading for the fatigue traction test; (b) ε_{22} strain component in one element near the crack tip with respect to the load.

respect to the mesh size. In that case, a regular mesh has been employed on the geometry described in Fig. 4 (a). The algorithm 2 has been used. The regularization parameter is chosen as $l = 0.01$ mm and the load increment as $\overline{U} = 10^{-5}$ mm. The results are provided in Fig. 7, demonstrating the convergence.

Finally, we investigate the capability of the split algorithm to handle auto-contact in a fatigue crack propagation. For this purpose, the same initial domain as described in Fig. 4 (a) is used, but traction conditions are prescribed, i.e. $y-$ displacements are prescribed while $x-$displacements are free. Here again, the algorithm 2 has been used. The evolution of the prescribed displacements is depicted in Fig. 8 (a). In figure 8 (b), the ε_{22} strain component in one element located just near the crack tip is plotted with respect to the resultant force on the upper end of the domain. We can note that the split algorithm is able to predict the progressive damage of the material in the case of fatigue crack.

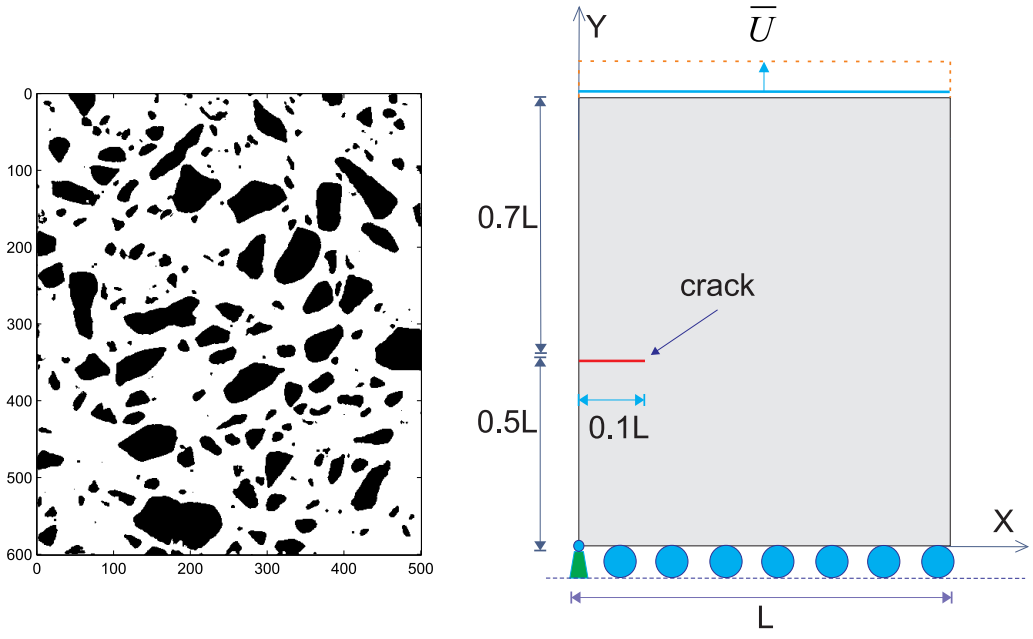

Figure 9. Traction test of a microtomography image-based mortar sample in 2D: (a) geometry of the phases; (b) geometry of the domain and boundary conditions.

5.2 Traction test of a microtomography image-based mortar sample in 2D

The purpose of the next series of test is to demonstrate the potential of the phase field method to handle highly complex microstructures such as those arising from microtomography images of real materials. The different examples have then been selected as tough and challenging problems for crack propagation.

In this example, we consider a model of mortar made of cement paste and sand particles. The geometry of the microstructure has been obtained by segmentation of a microtomography image. The data were kindly provided by Assistant Professor Sylvain Meille and Dr. Ing. Jerome Adrien, MATEIS laboratory-UMR CNRS, INSA Lyon, University of Lyon, France. The geometry of the inclusions in the model is described in Fig. 9 (a).

The domain contains an initial crack of length $a = 0.1L$, $L = 1$ mm, which is here defined by prescribing nodal values of the phase field $d(\mathbf{x}) = 1$ for the nodes on the crack. On the lower end ($y = 0$), the $y-$displacements are blocked, while the $x-$displacements are free. The node ($x = 0$), ($y = 0$) is blocked. On the upper end, the $x-$displacements are free, while the $y-$displacements are prescribed, with an increasing value of $\overline{U}$ during the simulation. Plane strain is assumed.

Three models are considered and each of them was obtained by segmenting the

original image rescaled to three different resolutions. In each case, the voxel data are transferred into a regular grid of square domains associated with voxels, each divided into 2 3-nodes elements. The models contains 125×150, 250×300 and 500×600 elements, respectively. Fig. 9 (a) shows the discretization associated with the last case. In this figure, white and black colors refer to matrix and inclusions, respectively. The material is a mortar composed of a cement paste (matrix) and sand (inclusions). The chosen material parameters of each phase are: $E_i = 30$ GPa, $\nu_i = 0.3$ (inclusions) and $E_m = 10$ GPa, $\nu_m = 0.2$ (matrix). The fracture toughness is $g_c = 250$ N/m. These numerical values have been chosen as the experimental ones described in [41], [31]. In all the examples of the present work, we have used the same g_c for all materials when two phases are involved in the microstructure. The computation is performed with monotonic displacement increments of $\overline{U} = 10^{-4}$ mm during the first 65 load increments and $\overline{U} = 5.10^{-6}$ mm during the last 500 increments corresponding to the softening part of the curve. The length scale parameter is chosen as $l = 0.016$ mm. The crack evolution for the different discretizations associated with different segmentations cases is depicted in Fig. 10.

We can note that the crack path is not much sensitive to the mesh refinement, despite of the highly heterogeneous nature of the microstructure and the large number of inclusions, with complex geometries and a wide span of sizes. A comparison of the load/displacement curves for the three cases is depicted in Fig. 11. A convergence of the different responses is observed for the different refined models. We can conclude that the phase field method is a promising tool for crack propagation in highly heterogeneous materials models obtained from microtomography images, mostly thanks to the weak dependency on the mesh refinement.

5.3 Shear test of a microtomography image-based mortar sample in 2D

In this example, we consider another slice taken from the same 3D microtomography image than in the previous example. The dimensions of the sample are the same as previously. However, the load here consists of shear conditions, as described in Fig. 12 (b). The geometry of the phases is described in Fig. 12 (a). On the lower end ($y = 0$), the $y-$displacements and the $x-$displacements are blocked. On the upper end, the y-displacements are blocked, while the x-displacements are prescribed, with an increasing value $\overline{U}$ during the simulation. The parameter $l = 0.016$ mm.

Here again, the same three resolutions as in the previous example are considered. The material parameters are the same as in the previous example. The crack evolution for the different segmentation cases is depicted in Fig. 13.

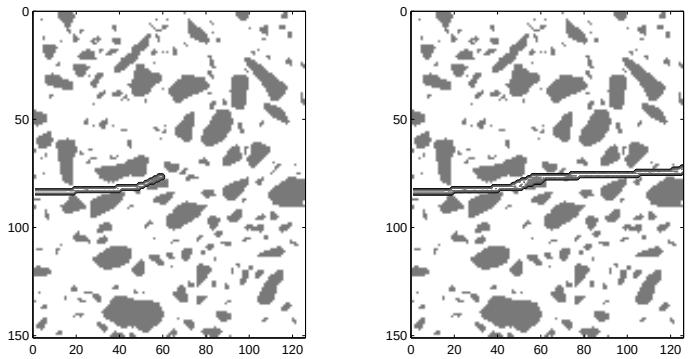

125×150

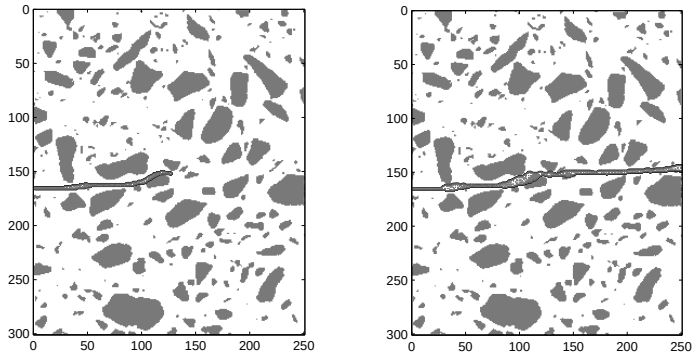

250×300

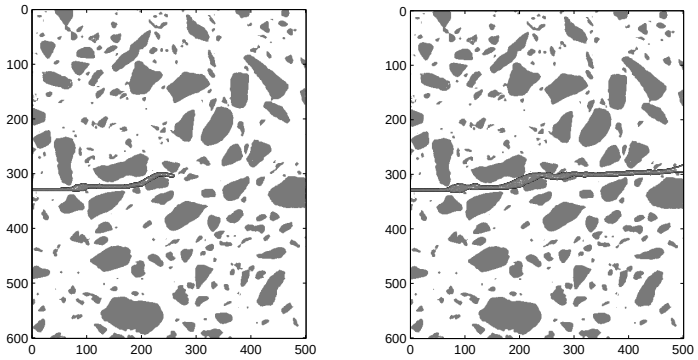

500×600

Figure 10. Traction test of a 2D microstructure defined by microtomography image, crack propagation for lower end displacement $\overline{U} = 0.008$ mm (left) and $\overline{U} = 0.00845$ mm (right). From up to down: 125×150, 250×300 and 500×600 elements discretizations.

Due to the shear load, we can note that the crack path deviates from the original orientation of the crack, as in the example of Fig. 5. In this case, the microstructure has been chosen such that one inclusion is in the path of the crack, to evidence the capability of the technique to propagate cracks in highly heterogeneous microstructures. No strong difference is noticed for the crack

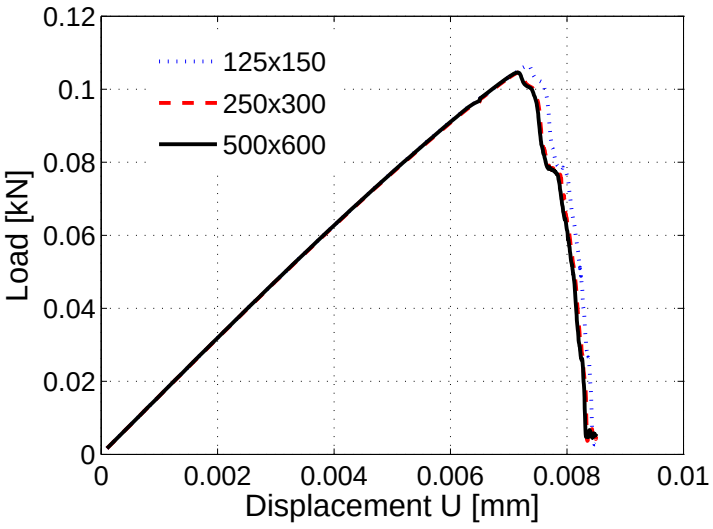

Figure 11. Load-deflection curve for the three segmentations of microtomography image-based models of mortar samples.

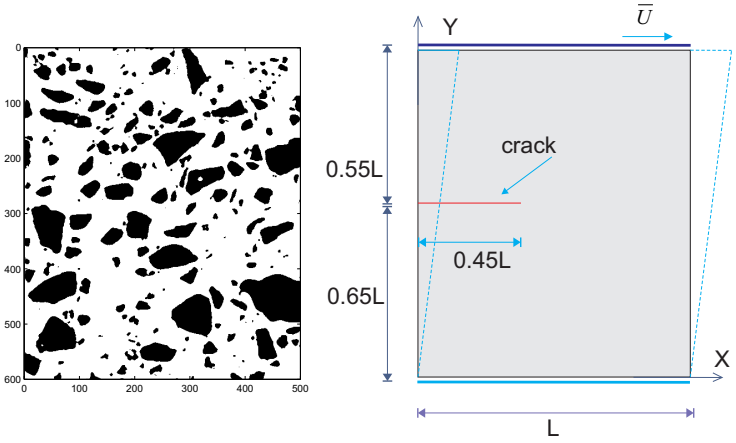

(a) (b)

Figure 12. Shear test of a microtomography image-based mortar sample in 2D: (a) geometry of the phases; (b) geometry of the domain and boundary conditions

path with the different resolutions. The comparison of the load/displacement curves for the three cases is depicted in Fig. 14. The load curve is found to converge to the value of the finest resolution. The step-like look of the curve is due to the fact that the crack passes through some inclusions during the loading.

5.4 Compression test of a microstructure with uniformly distributed pores

In this next example, a microstructure made of plaster containing periodically distributed holes is considered. This example has been studied numerically

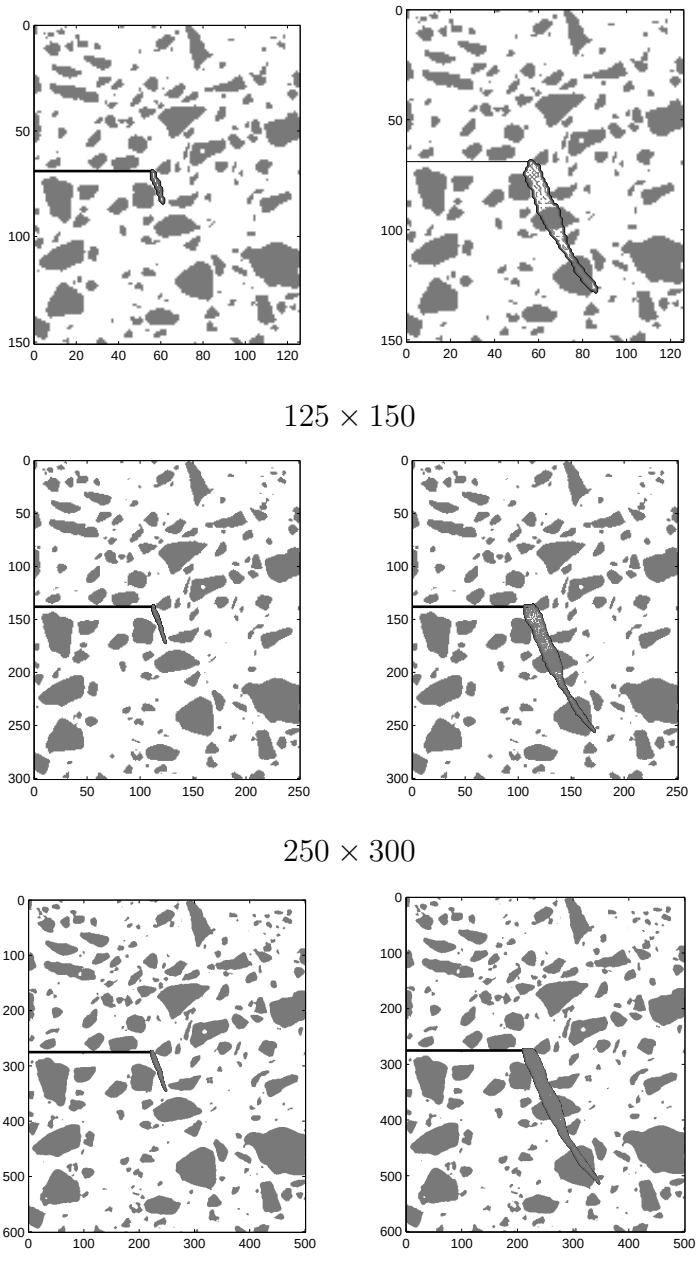

Figure 13. Shear test of a 2D microstructure, crack propagation for lower end displacement $\overline{U} = 0.0175$ mm (left) and $\overline{U} = 0.0235$ (right). From up to down: 125×150, 250×300 and 500×600 elements discretizations.

and experimentally in [52,54]. The domain, containing 23 holes with diameter $d = 0.2$ mm, as depicted in Fig. 15, is subjected to compression. The dimension of the sample is $L = 1$ mm (see figure 15).

The domain is meshed with elements whose characteristic size is $h \approx 6.10^{-3}$ mm, involving 299893 triangular elements. The properties of the matrix are

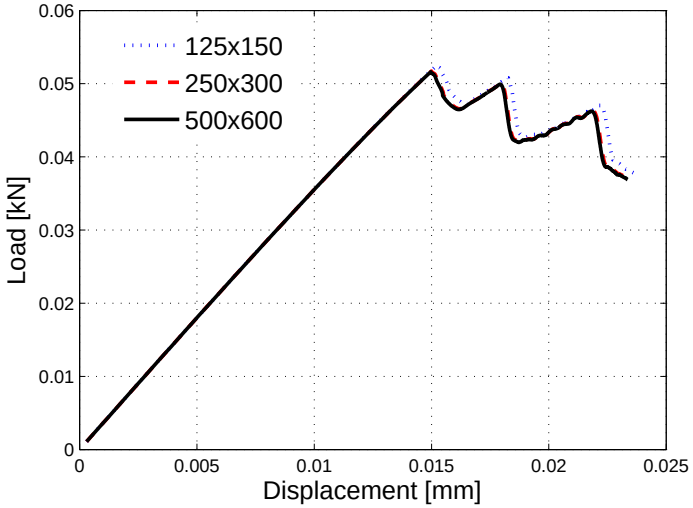

Figure 14. Shear test of a microtomography image-based mortar sample in 2D: load deflection curves for the three resolutions.

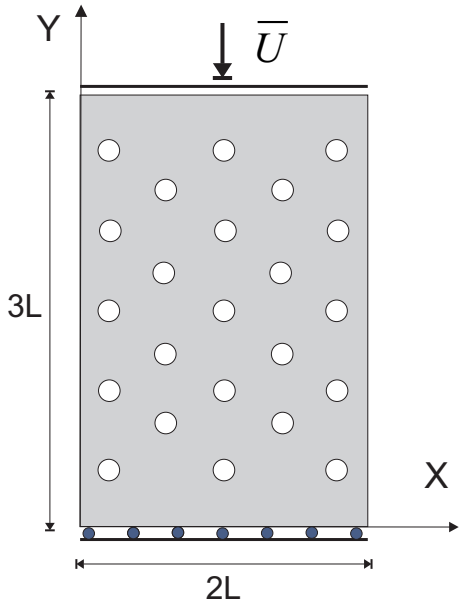

Figure 15. Compression test of a plate with regular distribution of holes: geometry of the domain and boundary conditions.

$E = 12$ GPa, $\nu = 0.3$ and $g_c = 1.4$ N/m. Monotonic compressive displacement increments of $\overline{U} = -1.5.10^{-4}$ mm is prescribed for the first 100 load increments and $\overline{U} = -3.10^{-5}$ mm in last 700 load increments. The length scale parameter is chosen as $l = 0.012$ mm. In Fig. 16, the evolution of the crack patterns with the a MFPA^{2D} simulation conducted in [54] are compared. The method captures the vertical crack propagation observed in the experiments performed in [52,50] and in the simulations performed in [54]. The corresponding load curve is provided in Fig. 17. This example illustrates the capability of the method to nucleate cracks from undamaged microstructure, with correct

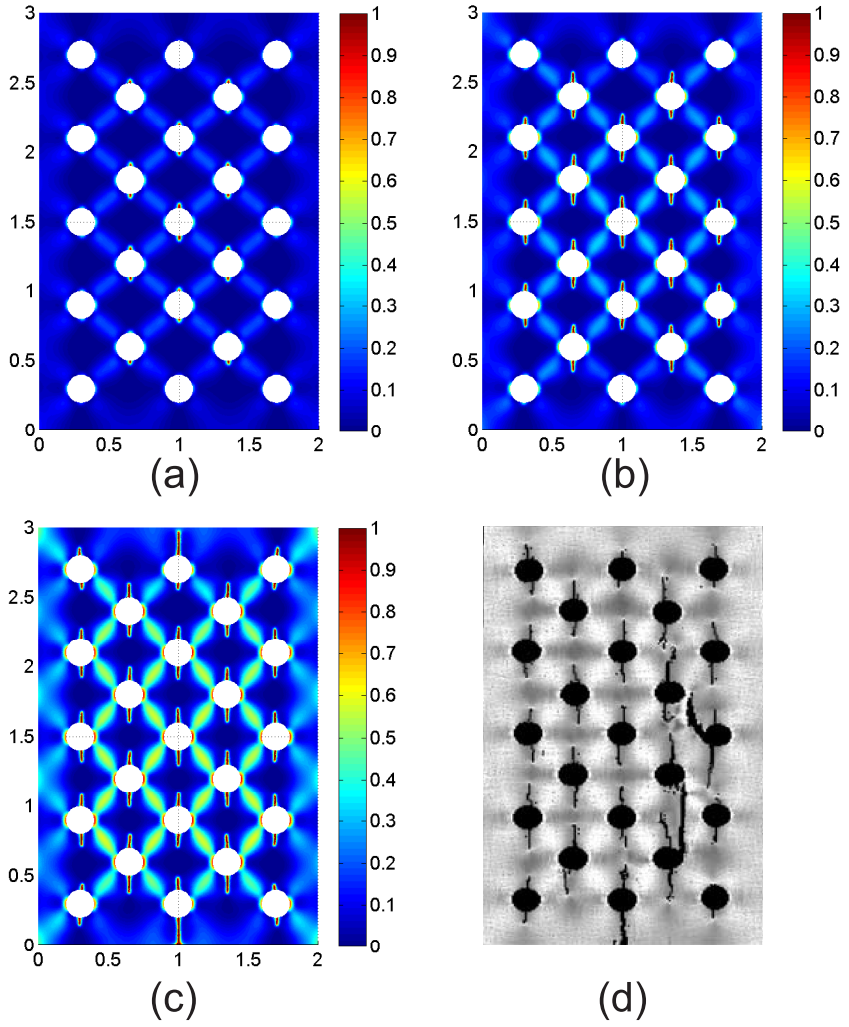

Figure 16. Compression test of a plate with regular distribution of holes: crack morphology field $d(\mathbf{x})$ at prescribed displacements: (a) $\overline{U} = 22.10^{-3}$ mm; (b) $\overline{U} = 26.10^{-3}$ mm; (c) and (d) $\overline{U} = 33.10^{-3}$ mm. The crack distribution depicted in (d) has been obtained by MFPA^{2D} simulation [54].

prediction of the crack path following the nucleation.

5.5 Compression test of a 3-phase microstructure without pre-existing cracks

In this example, a microtomography-based microstructure of a three-phases porous cementitious material is under consideration. The studied material is an EPS lightweight concrete [42], made from quartz sand and EPS beads embedded in a cement matrix. A microtomography image was recorded in about 45 min using an XRCT laboratory scanner available at Laboratoire Navier, with a voxel size of 15 μm. The grey level image was segmented in order to separate the three phases of the microstructure. The dimension of

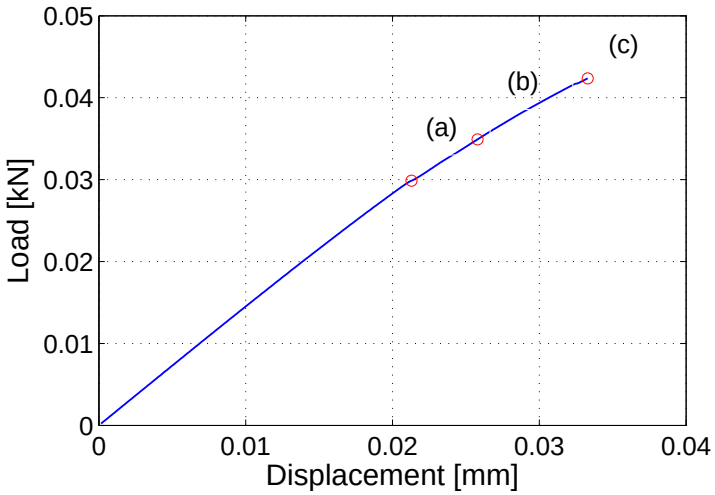

Figure 17. Compression test of a plate with regular distribution of holes: load-deflection curve.

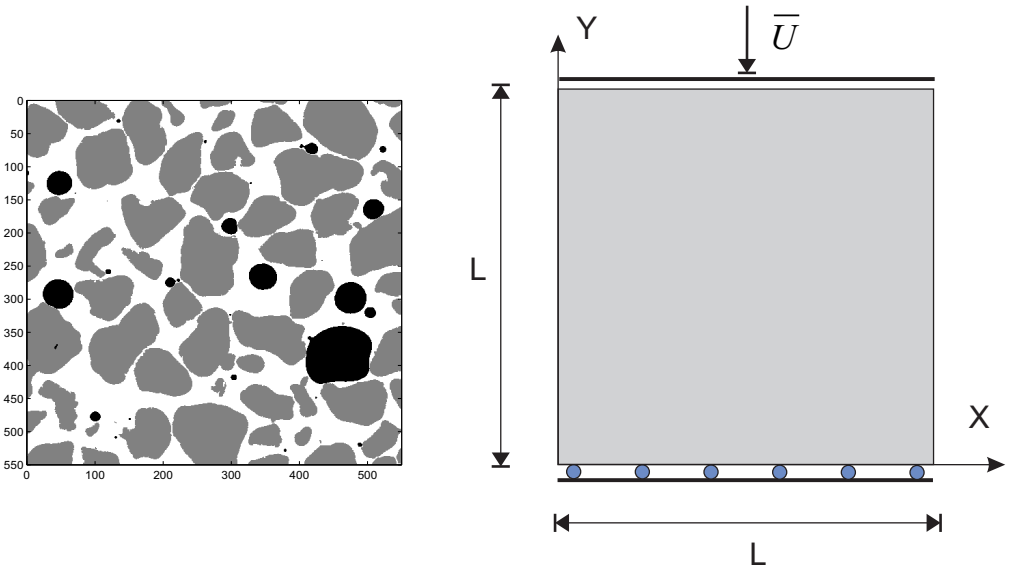

Figure 18. Compression test of a microtomography image-based model of porous cement based material: (a) microstructure: the white, grey and black phases correspond to matrix, inclusions and pores, respectively; (b) geometry of the domain and boundary conditions.

the sample is $L = 1$ mm (see figure 18) (b). As depicted in the same figure, the white, grey and black phases correspond to matrix, inclusions and pores, respectively.

On the lower end, the $y-$displacements are blocked while the $x-$displacements are free. On the upper end, the $x-$displacements are free, while the y-displacements are prescribed at value of $\overline{U}$ which increases during the simulation. Plane strain is assumed. The model consists of 550×550 pixels, each associated

with a material property of matrix, inclusion or holes, according to the data obtained from the microtomography image segmentation. The voxel data are transferred into a regular grid of square domains associated with voxels, each divided into 2 3-nodes elements. The material parameters of inclusions and matrix are, respectively: $E_i = 30$ Gpa, $\nu_i = 0.3$, and $E_m = 10$ Gpa, $\nu_m = 0.2$. The pores are meshed and have elastic properties $E_p = 10^{-10}$ Gpa, $\nu_p = 10^{-10}$. The fracture toughness is $g_c = 250$ N/m, and assumed to be identical for the different phases. This assumption is made for all further examples. The simulation is performed with monotonic displacement increments of $\overline{U} = -10^{-4}$ mm during the first 110 load increments and $\overline{U} = -10^{-6}$ mm during the last 240 load increments which correspond to the propagation of the micro cracks. The length scale parameter is chosen as $l = 7.5.10^{-3}$ mm. In this example, the domain does not contain pre-existing cracks, and the the cracks first nucleate and then propagate with increase of the compressive load. The crack distribution evolution for different load increments is depicted in Fig. 19. The load-displacement curve is provided in Fig. 20. We can observe that several cracks are nucleated from the pores and can propagate either in the matrix or in the inclusions, with complex paths. When the microcracks start nucleating, the materials strength quickly drops. This example shows the potential of the method for describing microcracking, involving nucleation and complex crack patterns in real microstructures.

5.6 Traction test of a 3D microtomography image-based microstructure

In this last example, we consider the same microtomography-based image model as in section 5.5. However, we here use a fully 3D model. The geometry of inclusions in the model is described in Fig. 21 (a). The dimension of the sample is $L = 1$ mm.

The domain contains an initial crack of size $0.35 \times 0.3 \times 0.01$ mm^3 which is here defined by prescribing nodal values of the phase field $d(\mathbf{x}) = 1$ for the nodes on the crack. On the lower end ($z = 0$), the $z-$displacements are blocked, while the $x-$displacements and $y-$displacements are free. The node ($x = 0$), ($y = 0$), ($z = 0$) is blocked. On the upper end, the $x-$displacements and $y-$displacements are free, while the $z-$displacements are prescribed, with an increasing value of $\overline{U}$ during the simulation.

The model is directly obtained from segmentation of the original image. The voxel data are transferred into a regular grid of 8-node elements. The model contains $300 \times 300 \times 200$ elements. Fig. 21 (a) shows the discretization. In this figure, white and blue colors refer to cement paste matrix and sand inclusions, respectively. We have here replaced the pores in the previous image by sand inclusions using the same geometry. The material parameters of each phase

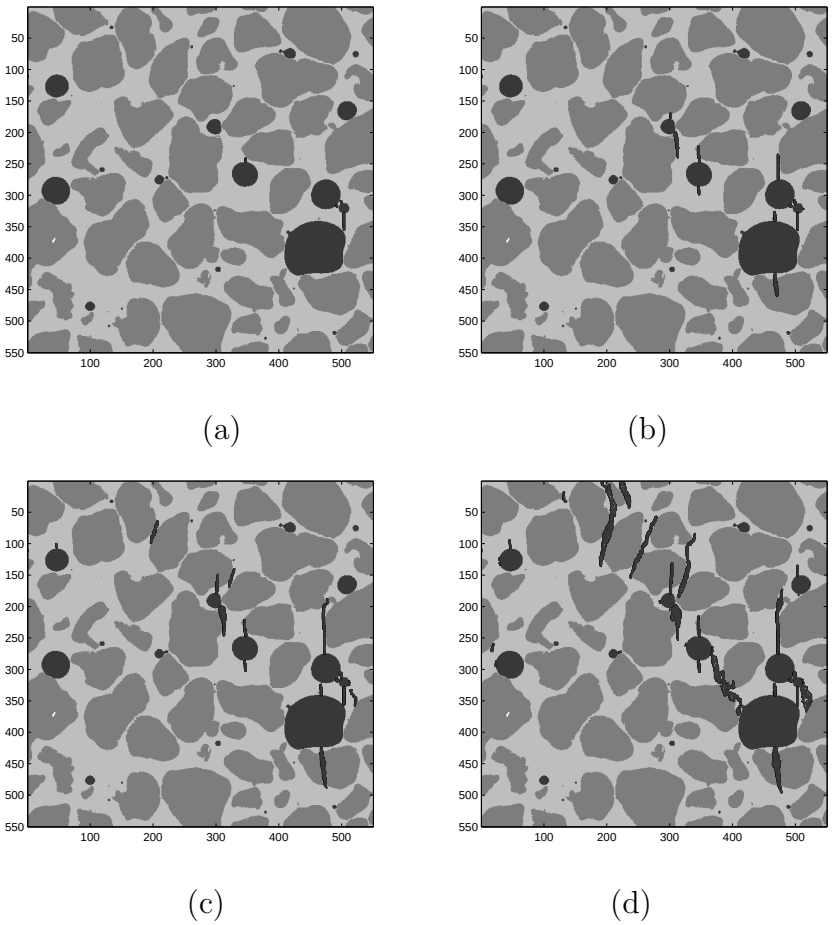

Figure 19. Compression test of a microtomography image-based model of cementitious material: crack propagation for (a) $\overline{U} = 20.5 \times 10^{-3}$ mm, (b) $\overline{U} = 23.5 \times 10^{-3}$ mm, (c) $\overline{U} = 24 \times 10^{-3}$ mm and (d) $\overline{U} = 25 \times 10^{-3}$ mm.

are: $E_i = 30$ GPa, $\nu_i = 0.3$, $E_m = 10$ GPa, $\nu_m = 0.2$. The fracture toughness is $g_c = 50$ N/m for both materials. The computation is performed with monotonic displacement increments of $\overline{U} = 10^{-4}$ mm during the 105 load increments and $\overline{U} = 10^{-5}$ mm during the last 90 load increments corresponding to the softening part of the curve. The length scale parameter is chosen as $l = 7.5.10^{-2}$ mm. The crack evolution is depicted in Fig. 22 and the stress-deflection curve is depicted in Fig. 23. Here, we demonstrate the capability of the method to describe 3D, multiple cracks propagation and interaction in image-based microstructure, up to the failure of the sample.

5.7 Computational times

Finally, a summary of the computational times for the different examples is reported in table 1. For all cases, a workstation with 8 cores, 144 Go Ram and 3.47 GHz processor was used. The present code has been implemented in

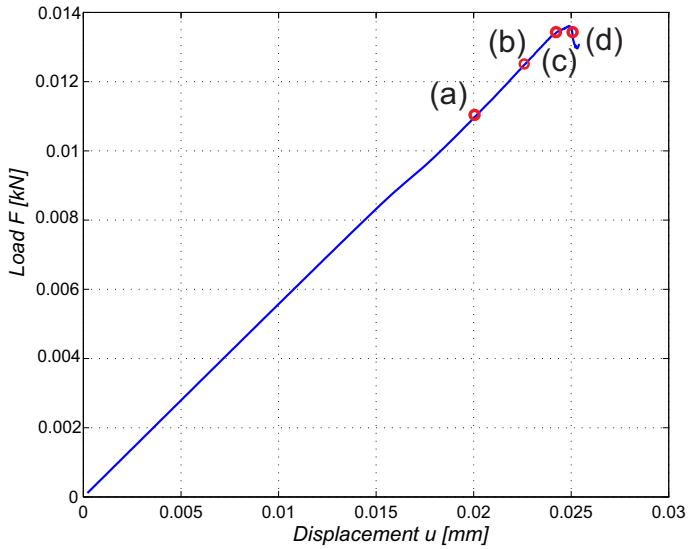

Figure 20. Compression problem: stress-deflection curve.

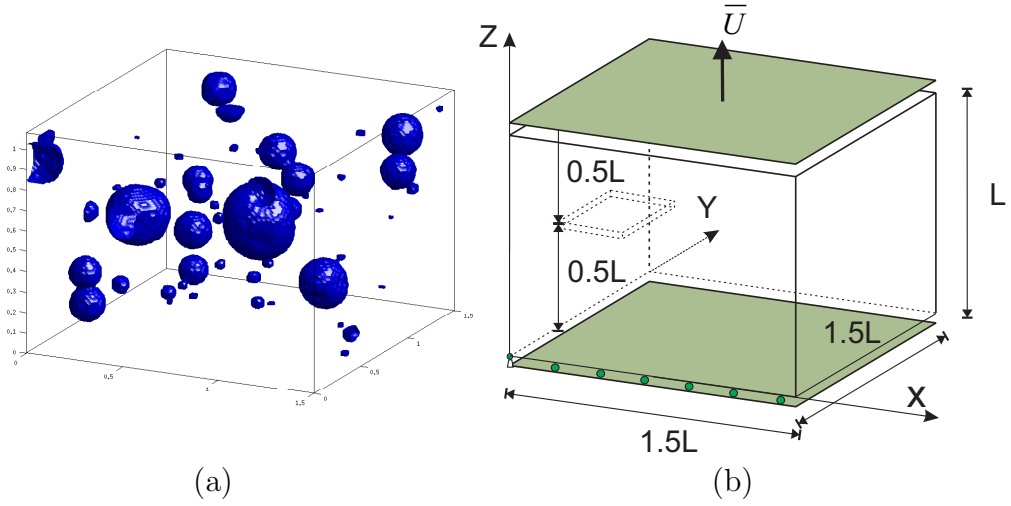

Figure 21. Traction test of a microtomography image-based concrete sample in 3D: (a) geometry of the phases; (b) geometry of the domain and boundary conditions.

Matlab ®.

6 Conclusion

In the present work, the phase field method has been applied for the first time to the analysis of brittle fracture in highly heterogeneous material models from direct imaging of their microstructure. The main procedure follows the works of Miehe et al.[37], with a modified algorithm to handle the damage only due to traction. For this purpose, a shifted algorithm was introduced, where

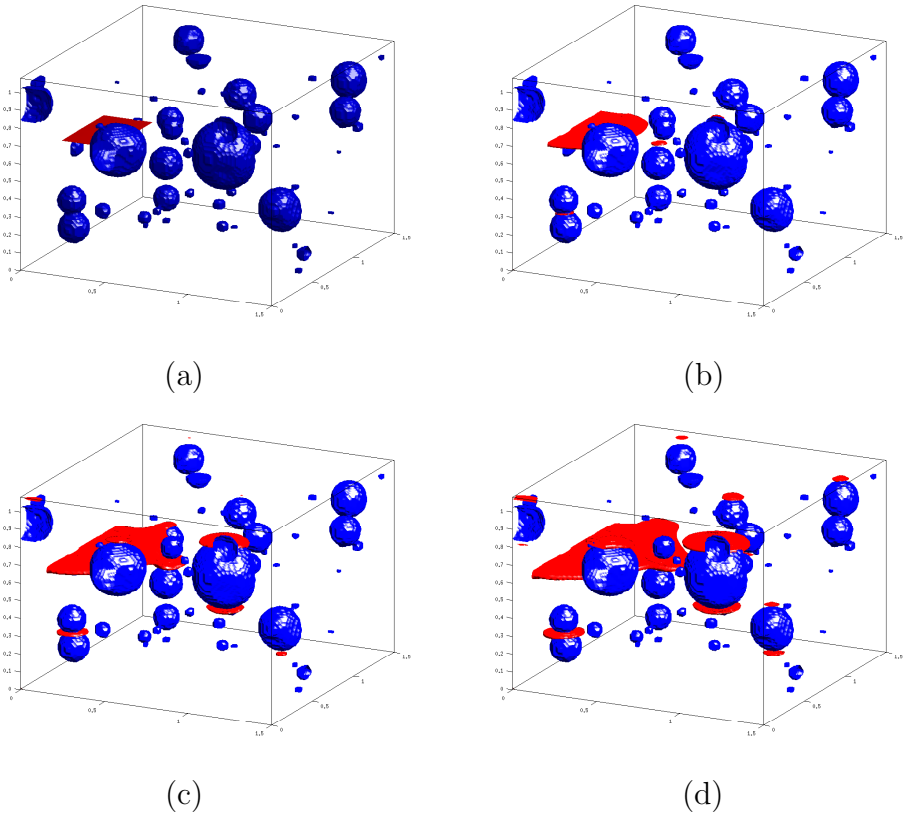

Figure 22. Traction test of a 3D microstructure defined from microtomography image, crack propagation for lower end displacement (a) : $\overline{U} = 0$ mm , (b) : $\overline{U} = 11 \times 10^{-3}$ mm, (c) : $\overline{U} = 11.2 \times 10^{-3}$ mm and (d) : $\overline{U} = 11.3 \times 10^{-3}$ mm.

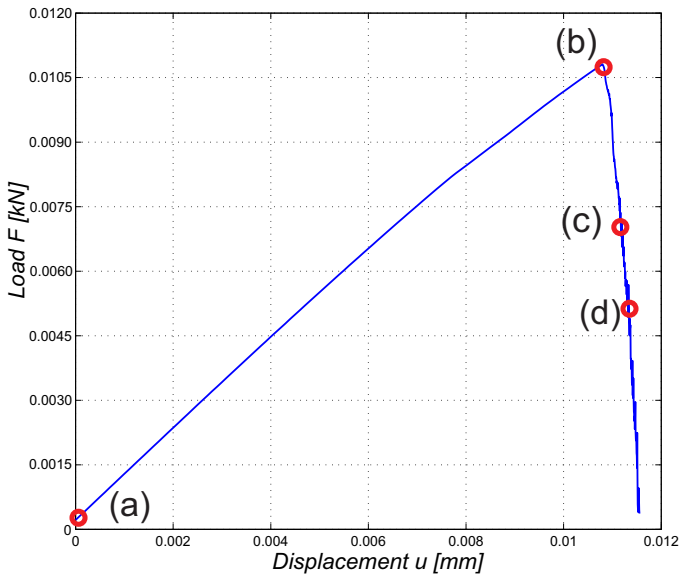

Figure 23. Tension test of a 3D microstructure defined from microtomography image: stress-deflection curve.

Problem	Nb. elements	Nb. load increments	CPU time for one load increment (s)	Total simulation time (h)
2D shear crack	74418	1200	10	3.34
2D tensile crack				
125×150	38052	350	4	0.4
2D tensile crack				
250×300	151102	350	18	1.75
2D tensile crack				
500×600	602202	350	80	7.78
2D shear crack				
125×150	38052	600	4.5	0.75
2D shear crack				
250×300	151102	600	19	3.17
2D shear crack				
500×600	602202	600	82	13.67
3 phases	607202	410	93	10.6
23 holes	303930	800	53	11.78
3D tensile crack	18.10^6	195	4131	224

Table 1
Computational times for the different examples

the compression/traction split of the strain tensor is performed in a previous load increment of the time-stepping, avoiding costly linearization procedures to the displacement problem, and allowing increasing load increments to save computational times. The obtained numerical tool allows simulating crack nucleation and crack propagation for arbitrary complexity of microstructures and for multiple cracks, in both 2D and 3D. Furthermore, as the present method is naturally based on a regularized representation of the crack surfaces, no significant mesh dependence has been noticed, which is highly recommended in voxel-based models, where the choice of the resolution is not always possible. There are many potential extensions for this work. First, the damage model associated with compression requires extensions to be more realistic. Secondly, many comparisons with experiments are now possible, and allows identification of the parameters related to the damage model, such as g_c, and the influence of the regularization parameter l in the identification process.

7 Aknowledgement

The support this work enjoys from LABEX "Multi-Scale Modelling & Experimentation of Materials for Sustainable Construction" (MMCD), through "ANR Investments for the Future program" ANR-11-LABX-022-01 is gratefully aknowledged. The authors also thank Assistant Professor Sylvain Meille and Dr. Ing. Jerome Adrien, MATEIS laboratory- UMR CNRS, University of Lyon, CNRS INSA-Lyon, France, who kindly provided the microtomography data used in example of sections 5.2 and 5.3. Finally, we are grateful to Prof. Karim Miled, professor at Ecole Nationale d'Ingénieurs de Tunis (ENIT), Tunisia, for providing us the cement paste samples used to obtain the microtomography image based models of 3D microstructures.

References

[1] A. Abdollahi and I. Arias. Phase-field modeling of crack propagation in piezoelectric and ferroelectric materials with different electromechanical crack conditions. *J. Mech. Phys. Solids*, 60:2100–2126, 2012.

[2] L. Ambrosio and V.M. Tortorelli. Approximation of functionals depending on jumps by elliptic functionals via Γ-convergence. *Comm. Pure Appl. Math.*, 43:999–1036, 1990.

[3] L. Ambrosio and V.M. Tortorelli. On the approximation of free discontinuity problems. *Boll. U.M.I.*, 6-B:105–123, 1992.

[4] H. Amor, J.-J. Marigo, and C. Maurini. Regularized formulation of the variational brittle fracture with unilateral contact: Numerical experiments. *J. Mech. Phys. Solids*, 57(8):1209–1229, 2009.

[5] T. Belytschko and T. Black. Elastic crack growth in finite elements with minimal remeshing. *Int. J. Numer. Meth. Eng.*, 45:601–620, 1999.

[6] A. Benallal and J.-J. Marigo. Bifurcation and stability issues in gradient theories with softening. *Model. Simul. Mater. Sci. Eng.*, 15:S283–S295, 2007.

[7] P.E. Bernard, N. Moës, and N. Chevaugeon. Damage growth modeling using the thick level set (TLS) approach: Efficient discretization for quasi-static loadings. *Comput. Meth. Appl. Mech. Eng.*, 233:11–27, 2012.

[8] B. Bourdin. Numerical implementation of the variational formulation of quasi-static brittle fracture. *Interface Free Bound.*, 9:411–430, 2007.

[9] B. Bourdin, G.A. Francfort, and J.J. Marigo. Numerical experiments in revisited brittle fracture. *J. Mech. Phys. Solids*, 48:797–826, 2000.

[10] B. Bourdin, G.A. Francfort, and J.J. Marigo. *The Variational Approach to Fracture*. Springer-Verlag, Berlin, 2008.

[11] B. Bourdin, C. Larsen, and C. Richardson. A time-discrete model for dynamic fracture based on crack regularization. *Int. J. Fract.*, 168:133–143, 2011.

[12] D.P. Braides. *Approximation of Free Discontinuity Problems*. Springer Verlag: Berlin, 1998.

[13] D.P. Braides. Γ-*Convergence for Beginners*. Oxford University Press: New York, 2002.

[14] M. Buliga. Energy minimizing brittle crack propagation. *J. Elast.*, 52:201–238, 1999.

[15] G. Camacho and M. Ortiz. Computational modelling of impact damage in brittle materials. *Int. J. Solids Struct.*, 33:2899–2938, 1996.

[16] F. Cazes and N. Moës. Comparison of a phase-field model and of a thick level set model for brittle and quasi-brittle fracture. *Int. J. Numer. Methods Eng.*, In press, 2015.

[17] François Cuvelier, Caroline Japhet, and Gilles Scarella. An efficient way to perform the assembly of finite element matrices in matlab and octave. *INRIA Research Report*, 2013.

[18] C. Daux, N. Moës, J. Dolbow, and T. Belytschko. Arbitrary branched and intersecting cracks with the extended finite element method. *Int. J. Num. Meth. Eng.*, 48:1741–1760, 2000.

[19] B.P. Flannery, H.W. Deckman, W.G. Roberge, and K.L. Damico. 3-dimensional X-ray microtomography. *Science*, 487:1439–1444, 1987.

[20] G.A. Francfort and J.J. Marigo. Revisiting brittle fracture as an energy minimization problem. *J. Mech. Phys. Solids*, 46(8):1319–1342, 1998.

[21] M. Frémond and B. Nedjar. Damage, gradient of damage and principle of virtual power. *Int. J. Sol. Struct.*, 33:1083–1103, 1996.

[22] L.B. Freund. *Dynamic Fracture Mechanics*. Cambridge University Press, Cambridge, 1990.

[23] A. Gravouil, N. Moës, and T. Belytschko. Non-planar 3d crack growth by the extended finite element and level sets-partii: level set update. *Int. J. Numer. Meth. Eng.*, 53(11):2569–86, 2002.

[24] A.A. Griffith. The phenomena of rupture and flow in solids. *Phil. Trans. Royal Soc. Lond. A*, 221:163–198, 1921.

[25] M.E. Gurtin. On the energy release rate in quasistatic elastic crack propagation. *J. Elasticity*, 9(2):187–195, 1979.

[26] M.E. Gurtin. Thermodynamics and the griffith criterion for brittle fracture. *Int. J. Solids Struct.*, 15:553–560, 1979.

[27] M. Hofacker and C. Miehe. A phase field model of dynamic fracture: Robust field updates for the analysis of complex crack patterns. *Int. J. Numer. Meth. Eng.*, 93:276–301, 2013.

[28] M. Holl, T. Rogge, S. Loehnert, P. Wriggers, and R. Rolfes. 3D multiscale crack propagation using the XFEM applied to a gas turbine blade. *Comput. Mech.*, 53:173–188, 2014.

[29] D.B.P. Huynh and T. Belytschko. The extended finite element method for fracture in composite materials. *Int. J. Num. Meth. Eng.*, 77:214–239, 2009.

[30] A. Ingraffea and V. Saouma. Numerical modelling of discrete crack propagation in reinforced and plain concrete. In *In: Sih, G., Di Tommaso, A. (Eds.), Fracture Mechanics of Concrete. Martinus Nijhoff Publishers*, pages 171–225, Dordrecht, 1984.

[31] C. Jaeger. *Rock mechanics and engineering.* Cambridge University Press, 1979.

[32] M. Jirasek. Nonlocal models for damage and fracture: comparison of approaches. *Int. J. Solids Struct.*, 35:4133–4145, 1998.

[33] M. Kikuchi, Y. Wada, Y. Shintaku, K. Suga, and Y. Li. Fatigue crack growth simulation in heterogeneous material using s-version FEM. *Int. J. Fatigue*, 58, 2014.

[34] T. Liebe, P. Steinmann, and A. Benallal. Theoretical and computational numerical aspects of a thermodynamically consistent framework for geometrically linear gradient damage. *Comput. Meth. Appl. Mech. Eng.*, 190:6555–6576, 2001.

[35] E. Lorentz and A. Benallal. Gradient constitutive relations: numerical aspects and applications to gradient damage. *Comput. Meth. Appl. Mech. Eng.*, 194:5191–5220, 2005.

[36] G. Dal Maso. *An Introduction to* Γ*-Convergence.* Birkhäuser Verlag: Boston, 1993.

[37] C. Miehe, M. Hofacker, and F. Welschinger. A phase field model for rate-independent crack propagation: Robust algorithmic implementation based on operator splits. *Comput. Meth. Appl. Mech. Eng.*, 199:2776–2778, 2010.

[38] C. Miehe and M. Lambrecht. Algorithms for computation of stresses and elasticity moduli in terms of seth-hill's family of generalized strain tensors. *Comm. Num. Meth. Engng.*, 17:337–353, 2001.

[39] C. Miehe, F. Welschinger, and M. Hofacker. A phase field model of electromechanical fracture. *J. Mech. Phys. Solids*, 58:1716–1740, 2010.

[40] C. Miehe, F. Welschinger, and M. Hofacker. Thermodynamically consistent phase-field models of fracture: Variational principles and multi-field FE implementations. *Int. J. Numer. Meth. Eng.*, 83:1273–1311, 2010.

[41] K. Miled, R. Le Roy, K. Sab, and C. Boulay. ompressive behavior of an idealized eps lightweight concrete: size effects and failure mode. *Mech. Mater.*, 36:1031–1046, 2004.

[42] K. Miled, K. Sab, and R. Le Roy. Particle size effect on eps lightweight concrete compressive strength: Experimental investigation and modelling. *Mech. Mater.*, 39:222–240, 2007.

[43] N. Moës, J. Dolbow, and T. Belytschko. A finite element method for crack growth without remeshing. *Int. J. Numer. Meth. Eng.*, 46(1):131–156, 1999.

[44] N. Moës, A. Gravouil, and T. Belytschko. Non-planar 3D crack growth by the extended finite element and level sets-part-i: mechanical model. *Int. J. Numer. Meth. Eng.*, 53(11):2549–68, 2002.

[45] D. Mumford and J. Shah. Coptimal approximations by piecewise smooth functions and associated variational problems. *Commun. Pure Appl. Math.*, 42:577–685, 1989.

[46] B. Moran T. Belytschko N. Sukumar, N. Moës. Extended finite element method for three-dimensional crack modeling. *Int. J. Num. Meth. Eng.*, 48(11):1549–70, 2000.

[47] R.H.J. Peerlings, R. de Borst, W.A.M. Brekelmans, and H.P.J. de Vree. Gradient-enhanced damage for quasi-brittle materials. *Int. J. Num. Meth. Eng.*, 39(39):3391–3403, 1996.

[48] K. Pham and J.-J. Marigo. The variational approach to damage: I. the foundations. *C. R. Mecanique*, 338:191–198, 2010.

[49] G. Pijaudier-Cabot and Z. Bazant. Nonlocal damage theory. *J. Eng. Mech.*, 113:1512–1533, 1987.

[50] D. Leguillon R. Le Roy R. Romani, M. Bornert and K. Sab. Detection of crack onset in double cleavage drills specimens of plaster under compression by digital image correlation - theoretical predictions based on a coupled criterion. *Eur. J. Mech. A-Solid*, 51:172–182, 2015.

[51] Y.R. Rashid. Analysis of reinforced concrete pressure vessels. *Nucl. Eng. Des.*, 7:334–344, 1968.

[52] R. Romani. *PhD Thesis, Rupture en compression des structures hétérogènes à base de matériaux quasi-fragiles.* PhD thesis, Université Pierre et Marie Curie, Paris VI, 2013.

[53] Yousef Saad. *Iterative methods for sparse linear systems.* Siam, 2003.

[54] C.A. Tang, R.H.C. Wong, K.T. Chau, and P. Lin. Modeling of compression-induced splitting failure in heterogeneous brittle porous solids. *Eng. Frac. Mech.*, 72:597–615, 2005.

[55] G. Ventura, E. Budyn, and T. Belytschko. Vector level-sets for description of propagating cracks in finite elements. *Int. J. Num. Meth. Eng.*, 58(10):1571–92, 2003.

[56] C. Verhoosel and R. de Borst. A phase-field model for cohesive fracture. *Int. J. Numer. Meth. Eng.*, 96:43–62, 2013.

[57] X.-P. Xu and A. Needleman. Numerical simulation of fast crack growth in brittle solids. *J. Mech. Phys. Solids*, 42(9):1397–1434, 1994.

[58] F. Zhou and J.F. Molinari. Dynamic crack propagation with cohesive elements: a methodology to address mesh dependency. *Int. J. Numer. Meth. Eng.*, 59:1–24, 2004.